



Stimulate the hidden catalysis potential and exposure of nickel site in NiSe@CNTs result in ultra-high HER/OER activity and stability

Hongyao Xue^a, Tongqing Yang^a, Ziming Zhang^a, Yixue Zhang^a, Zhihong Geng^b, Yan He^{a,*}

^a College of Electromechanical Engineering, School of Polymer Science and Engineering Qingdao University of Science and Technology, Qingdao 266061, Shandong, PR China

^b School of Literature, Journalism and Communication, Qingdao University, Qingdao 266061, Shandong, PR China

ARTICLE INFO

Keywords:

Heterostructures
Hidden catalysis potential
Electrocatalyst
 π -electron delocalization
Water splitting

ABSTRACT

We present an electrodeposition strategy to construct heterostructures nickel selenide (NiSe) and carbon nanotubes (CNTs), namely NiSe@CNTs, to tune the electronic structure of the Ni sites, thus stimulating the hidden catalytic potential of the Ni sites. As expected, the optimized NiSe@CNTs exhibits unprecedentedly ultra-high activity for HER (27 mV at 10 mA cm⁻²) and OER (145 mV at 100 mA cm⁻²) and outstanding long-term durability (730 h). Based on the systematic characterization and DFT results, the Ni sites with increased electron density induced by π -electron off-domain of CNTs not only greatly optimize the H⁺ adsorption kinetics but also reduce the energy barrier of the *O→*OOH step, demonstrating the enhanced intrinsic catalytic activity. Furthermore, the introduced CNTs not only avoid aggregation of nanoparticles but also reduce particle size, thus increasing the number of exposed Ni active sites. This study provides guidance for the exploration of catalysts with ultra-high activity and durability.

1. Introduction

Currently, hydrogen is considered an ideal alternative energy source due to its high energy density, storability, renewability and zero pollution [1–4]. To achieve highly efficient electrochemical water splitting for hydrogen production, it is an inevitable trend to construct cost-effective, highly active and stable electrocatalysts [5–7]. Nickel chalcogen (Group VIA elements) compounds are considered highly promising bifunctional nanomaterials owing to their tunable electronic structures, high-density state of d-electrons and high covalent degree of metal-anion bonding [8–11]. Among them, selenium with the electronic structure 4s² 4p⁴ and empty 4d orbitals presents a stronger metallicity and smaller ionization energy due to its lower electronegativity than oxygen and sulfur, so nickel selenides usually exhibit higher electrocatalytic efficiency than nickel oxides and nickel sulfides [12]. However, the electron-deficient Ni sites in pristine NiSe have insufficient adsorption and desorption capacity for hydrogen protons and oxygen-containing species, resulting in less-than-optimal activity [13]. Therefore, improving the electron density of the Ni sites is essential to enhance the catalytic activity of NiSe.

Considering the above problems, the construction of heterojunctions from NiSe and another phase can not only compensate for the

shortcomings of single-component NiSe, but also regulate the active site and electronic structure, thus optimizing the adsorption and desorption capacity for reaction intermediates on the catalyst surface [14,15]. Therefore, the constructing heterostructures strategy is considered an effective way to solve the lack of intrinsic activity for NiSe. For example, Lee et al. prepared a hierarchical heterostructure of CoFe-LDH@NiSe on NF, which displayed remarkable catalytic activity toward the overall water-splitting due to interfacial coupling [12]. Moreover, the synthesis of MoSe₂/NiSe-1 heterojunction nanocomposites greatly enhanced HER catalytic activity due to higher electron density and conductivity via the strong electronic synergistic interaction among the different interfaces [16]. Ray and coworkers constructed Ni₃S₂@NiSe/NF catalyst promoted better electron localization and faster charge transfer of the adsorbed charged species, resulting in excellent overall water splitting performance [17]. Although the aforementioned studies have affirmed the contribution of constructing heterostructures to improve the electrocatalytic performance of NiSe, the catalysis potential of the Ni sites was not fully exploited, resulting in its catalytic performance remaining below expectations. Therefore, the choice of suitable coordination material that can provide a large number of free electrons plays a crucial role in further exciting the full potential of the Ni sites.

In addition to the optimization of intrinsic activity, the modification

* Corresponding author.

E-mail address: heyang@qust.edu.cn (Y. He).

<https://doi.org/10.1016/j.apcatb.2023.122641>

Received 5 January 2023; Received in revised form 11 March 2023; Accepted 13 March 2023

Available online 15 March 2023

0926-3373/© 2023 Elsevier B.V. All rights reserved.

of insufficient active sites for NiSe should not be neglected [18]. The severe aggregation between nanoparticles not only prevented adequate contact between the active sites and electrolytes but also retarded the mass diffusion, leading to a decrease in electrocatalytic activity [19–21]. Thus, the study of how to avoid the aggregation of nanoparticles is also a challenge that we have to face. For CNTs, the π -electrons of carbon atoms form a large range of off-domain π -bonds with significant conjugation effects, and the electrons are free to move over a large range independent of individual carbon atoms, resulting in high charge mobility [22,23]. The heterostructures constructed based on CNTs can provide a convenient pathway for mass diffusion and fast electron transport, thus exhibiting high activity and stable electrocatalytic performance [24–26].

Herein, we establish monodisperse NiSe nanoparticles with a much small size of 10–15 nm supported on self-made CNTs for efficient electrochemical water splitting. Compared with the single-component NiSe nanoparticles, the introduced CNTs not only avoid the agglomeration of nanoparticles but also reduce their particle size, which helps to stabilize and increase the number of exposed active sites, thus improving the catalytic stability and activity. The interfacial effect between NiSe and CNTs in the heterostructure exacerbates the further π -electrons delocalization of CNTs, which leads to the localization of π -electrons at the Ni sites, making the local electron enrichment at the Ni sites. The increased electron density excites the hidden catalysis potential of the Ni sites in NiSe@CNTs, which greatly compensates for the lack of NiSe adsorption capacity for hydrogen protons and desorption capacity for all three oxygen-containing species, respectively, thus improving the intrinsic activity. Benefit from the further release of the intrinsic catalytic activity potential of the nickel sites and exposure of more active sites, the designed NiSe@CNTs exhibits ultra-high HER activity with a low overpotential of only 27 mV at 10 mA cm⁻² and unbelievable activity toward OER (overpotential of 145 mV to achieve 100 mA cm⁻²), which is superior to that of precious metals and almost all of the recently reported advanced catalysts. Moreover, it exhibits strong long-term stability of more than one month (730 h). Particularly, the NiSe@CNTs electrocatalyst demonstrates efficient water splitting in a two-electrode system with a cell voltage as low as 1.43 V at 10 mA cm⁻² with outstanding long-term stability for 350 h. The constructed catalyst can greatly improve the water splitting efficiency, which not only fundamentally solves the high energy consumption problem in the process of hydrogen from water splitting, but also promotes the process of industrial application.

2. Experimental sections

2.1. Synthesis of NiSe@CNTs

A mixture of CNTs, PVDF and acetylene black was prepared in a molar ratio of 8:1:1 and ultrasonicated for 30 min. The prepared mixture was evenly coated on nickel foam and dried in a vacuum drying oven at 60 °C for 6 h. Meanwhile, a 20 mmol L⁻¹ concentration of NiCl₂·6 H₂O, 20 mmol L⁻¹ concentration of SeO₂ and a concentration of 5 mmol L⁻¹ LiCl were made into an electrodeposition solution. Finally, the nickel foam electrode with carbon nanotubes was placed in the electrodeposition solution and the NiSe@CNTs/NF electrode was obtained by electrodeposition at -0.8 V for 800 s with the help of the three-electrode method.

2.2. Structural and morphological characterization

The crystallinity and purity of the as-prepared samples were evaluated qualitatively by thin film powder x-ray diffraction (XRD) using the Shimadzu XRD-6000 X-ray diffractometer with Cu-K ($\lambda = 1.5406$ Å) irradiation source. Furthermore, to confirm the chemical composition of the materials and learn about the bonding states of the species involved X-ray Photoelectron Spectroscopy (XPS) was performed using the

Thermo Scientific K-Alpha⁺ device with an Al-K α ($h\nu = 1486.6$ eV) excitation source. Raman spectra were collected with the aid of a microscope Raman system (Senterra, Bruker) with an excitation wavelength of 532 nm. Low power of 0.2 mW was chosen to avoid damage caused by laser radiation. Thermogravimetric analysis (TGA) was performed on a thermogravimetric analyzer (Netzsch Germany TG-209F3) in the air at a temperature rise rate of 10 °C min⁻¹. The surface wettability of catalysts was observed by the SL 200KS model optical contact angle meter and their pore size distribution and specific surface area were characterized by a 3 H-2000PS1 specific surface as well as pore size analysis instrument at 77 K. The micro-morphology and chemical composition were investigated by scanning electron microscopy (SEM) using the JEOL JSM-6. The Hitachi H-8100 transmission electron microscope (TEM) was employed to study structural information in greater detail.

2.3. Computational details

All DFT calculations were constructed and implemented in the Vienna ab initio simulation package (VASP). Using the electron exchange and correlation energy was treated within the generalized gradient approximation in the Perdew–Burke–Ernzerhof functional (GGA-PBE), the calculations were done with a plane-wave basis set defined by a kinetic energy cutoff of 450 eV. The long-range dispersion interactions between adsorbates and surface were treated by applying the DFT-D3 method developed by Grimme et al. The k-point sampling was obtained from the Monkhorst–Pack scheme with a $(3 \times 3 \times 1)$ mesh for optimization and electronic structure. The geometry optimization and energy calculation are finished when the electronic self-consistent iteration and force reach 10⁻⁵ eV and 0.02 eV Å⁻¹, respectively.

3. Results and discussion

3.1. External means to enhance catalytic activity

The synthesis procedure of NiSe@CNTs was schematically illustrated in Fig. 1a and the details of the synthesis were shown in the supporting information. The X-ray diffraction (XRD) patterns of NiSe/NF and NiSe@CNTs/NF electrodes were shown in Fig. 1b. The NiSe sample exhibits the characteristic diffraction peaks at 2 θ of 32.8, 44.4, 49.9, 59.6, 61.2 and 70.4°, corresponding to the (101), (102), (110), (103), (201) and (004) crystal planes of typical NiSe (JCPDS 02-0892), respectively [16,27]. Compared with NiSe, two new characteristic diffraction peaks of 26.3, 42.2, 44.3 and 50.4° appear at the XRD pattern of NiSe@CNTs/NF, which correspond well with the (002), (100), (101) and (004) facets of CNT (JCPDS 75-1621), demonstrating that it is composed of the NiSe and CNTs [28]. As shown in Fig. S1, the NiSe content in NiSe@CNTs was determined to be ~43.7 wt% by thermogravimetric analysis (TGA) in the air. The value is in general agreement with the elemental analysis results (Table S3). The SEM image of NiSe shows that a large number of active sites are masked due to the close alignment and aggregation of nickel selenide nanoparticles, which is an external factor contributing to the poor catalytic activity (Fig. 1c). As shown in Fig. 1d–e, after introducing NiSe on the CNTs network, these nanoparticles are uniformly dispersed and firmly fixed on the CNTs. As can be seen from the SEM images of NiSe and NiSe@CNTs, its particle size is about 10–15 nm, which is much smaller than that of the single component NiSe (Fig. S2). This is due to the fact that the introduced CNTs not only provide more growth sites for NiSe, but also compress its growth space resulting in a significantly smaller particle size than that of single component NiSe.

As displayed in Fig. 1f–g, the NiSe@CNTs heterogeneous structure can be further observed by the TEM test technique [29]. The HRTEM image shows that the crystalline planes with a lattice spacing of 0.18 nm correspond to the (102) crystalline planes of NiSe. It can be clearly seen from the TEM and HRTEM images that the two NiSe nanoparticles are

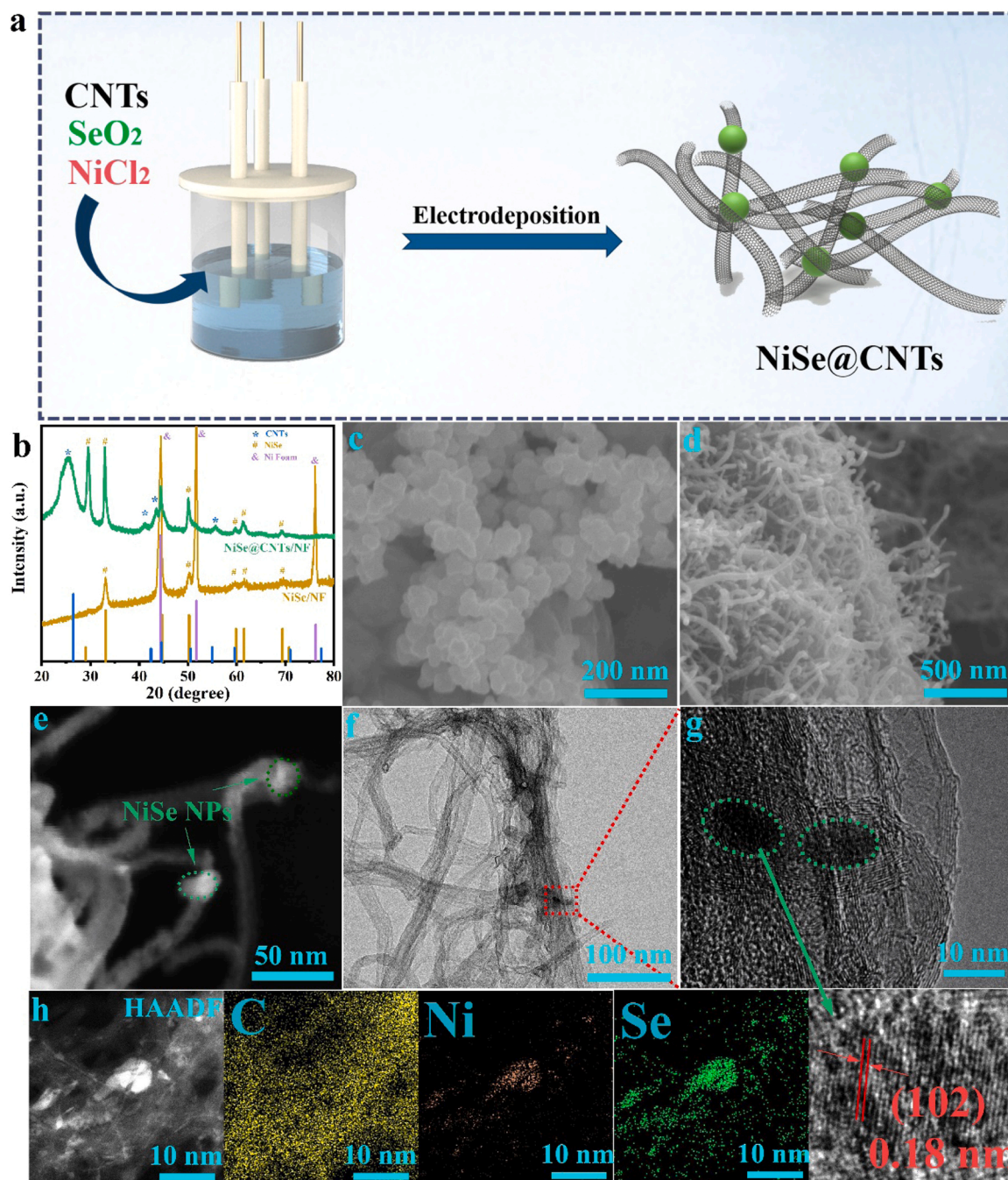


Fig. 1. (a) Schematic illustration of the preparation of NiSe@CNTs. (b) XRD patterns of NiSe and NiSe@CNTs. SEM images of (c) NiSe and (d,e) NiSe@CNTs. (f) TEM image and (g) HRTEM image of NiSe@CNTs. (h) HAADF-STEM and element mapping for NiSe@CNTs.

entangled and completely separated by multiple carbon tubes, further confirming the outstanding dispersion of the NiSe@CNTs heterogeneous structure. As shown in Fig. 1h, the element mapping results show that the NiSe@CNTs heterogeneous structure is composed of C, Ni and Se three elements, and the NiSe nanoparticles are wrapped by multiple carbon nanotubes. In addition, the results of hydrophilicity and specific surface area test further corroborate the above characterization results (Fig. S3-S4). As a way of external means of enhancing catalytic activity, the characterization results demonstrate that the CNTs not only avoid the agglomeration of nanoparticles but also reduce their particle size, which helps to stabilize and increase the number of exposed active sites, thus improving the catalytic stability and activity.

3.2. Internal means to enhance catalytic activity

In addition to increasing the number of exposed Ni active sites, stimulation of the intrinsic catalysis potential of each Ni site would lead to further enhancement of the catalytic activity. The CNTs with the extended π conjugation in the NiSe@CNTs heterogeneous structure increase the π -electrons delocalization and promote the electron localization of Ni sites in NiSe, leading to an increase in the electron density around Ni sites [30]. So, what is the role of Se in NiSe? Do other Group VIA elements, such as O in nickel oxide or S in nickel sulfide, play a more prominent role than Se? Since the electronegativity of Se is less than that of O and S, O and S in heterostructures are more likely to grab more electrons from CNTs than Se, which leads to the result that the electron

density of Ni sites on NiO/NiS is less than that of Ni sites on NiSe. This suggests that NiSe is more suitable than NiO or NiS for building heterostructures with CNTs to excite the catalytic activity potential of Ni sites.

In order to compare more visually the magnitude of the charge density around the Ni site, the Bader charges and charge density difference of the NiSe@CNTs, NiO@CNTs and NiS@CNTs heterogeneous structures were calculated, respectively [31,32]. As displayed in Fig. 2a, the Bader charge of Se site in NiSe@CNTs is significantly lower than that of NiO@CNTs and NiS@CNTs, which indicates that the Se sites grab the least number of electrons, resulting in a higher electron enrichment of Ni sites in NiSe@CNTs. The charge density difference results show that the construction of heterogeneous structures leads to charge transfer between NiSe (NiO or NiS) and CNTs, and more importantly, NiSe@CNTs exhibit stronger electron aggregation at the Ni site than NiO@CNTs and NiS@CNTs (Fig. 2b and Fig. 6b). Furthermore, comparing the work functions of NiSe, NiO, NiS and CNTs reveal that CNTs with the work function of 4.25 eV is significantly lower than that of NiSe (5.26 eV), NiO (5.02 eV) and NiS (5.13 eV). It is noteworthy that when two phases with different work functions are combined together, a potential difference is generated at the interface domain, which will further lead to electron redistribution and modulation of the electronic structure. As shown in Fig. 2c, electrons will be transferred from CNTs to NiSe, NiO and NiS until equilibrium is reached. Since the difference between NiSe and CNT is the largest, then the nickel selenide will undoubtedly get more electrons after establishing the heterogeneous structure [33]. Based on the above analysis, NiSe is undoubtedly a better choice than NiO or NiS for the construction of heterogeneous structures with CNTs for catalytic hydrogen and oxygen evolution.

To identify the surface elemental state and electronic structures of NiSe, CNTs and NiSe@CNTs, X-ray photoelectron spectroscopy (XPS) was carried out. As presented in Fig. S5a, the XPS survey spectrum displays that the NiSe@CNTs is a combination of NiSe and CNTs. In addition, the oxygen element may come from O₂ or CO₂ adsorbed on the sample surface or due to slight oxidation of the sample exposed to air [34]. In addition, the C 1 s peak of NiSe@CNTs is consistent with that of CNTs, which further indicates that it contains CNTs (Fig. S5b). The C 1 s peak of NiSe is attributed to the carbon signal contained in the instrument for calibration purposes [35]. As shown in Fig. 3a, the Ni 2p spectra of the NiSe and NiSe@CNTs display three parts: Ni³⁺ peak, Ni²⁺ peak and two satellite peaks [36,37]. Compared to the Ni 2p state in

NiSe, the characteristic peaks of both the Ni²⁺ and Ni³⁺ species of NiSe@CNTs shift toward lower binding energies by 0.5 eV [38]. Meanwhile, based on the Ni²⁺/Ni³⁺ peak areas, the molar ratios of Ni²⁺/Ni³⁺ are calculated to be 1.12 and 1.86 for the catalyst before and after constructing a heterogeneous structure, respectively. This implies that the construction of heterostructures leads to a lower valence state and higher electron density of the Ni sites, thus enhancing the adsorption of the catalytic reaction species [24]. The Se 3d high-resolution spectrum also is divided into three typical peaks as shown in Fig. 3b. The Se 3d_{3/2} and Se 3d_{5/2} two peaks of NiSe@CNTs also show a slight negative shift as compared to those of NiSe, which indicates that the interfacial effect between NiSe and CNTs in the heterostructure exacerbates the further π -electrons delocalization of CNTs [39].

X-ray absorption spectroscopy (XAS) measurements were conducted to gain more insight into the changes in both Ni and Se sites in the NiSe lattice before and after constructing the heterogeneous structure. [1] As shown in Fig. 3c, the Ni K-edge spectrum of NiSe@CNTs shifts to lower energy compared to NiSe, indicating a lower valence state of Ni. Furthermore, its white line intensity is lower than that of NiSe, which confirms that the interfacial effect between NiSe and CNTs in the heterostructure exacerbates the further π -electrons delocalization of CNTs, thus resulting in an increase in the electron density around the Ni sites, which is completely in accord with the above XPS results [40]. The electrons change around the Ni sites is further verified by the following Fourier transform curves of Ni K-edge EXAFS in R space (Fig. 3d). The main coordination peak for NiSe at 2.11 Å corresponds to the first coordination shell of the Ni-Se bond, which is close to the Ni-Ni scattering interaction of the Ni foil (2.18 Å), indicating its high metallicity [22]. Compared with the single-component NiSe, the main peak for NiSe@CNTs shifts to a smaller radial distance of 2.06 Å, demonstrating the contraction of the Ni-Se bond and the interfacial effect between NiSe and CNTs in the heterostructure effect on the local atomic arrangement of the Ni site [18]. Fig. 3e-f presents their Se K-edge XANES and Fourier transform EXAFS spectra, respectively. Compared to NiSe, the spectra of NiSe@CNTs shifts slightly higher energy, which is closer to that of Se foil, indicating that Se also gains a small fraction of electrons [41]. As shown in Fig. 3f, the Ni-Se bond length of NiSe@CNTs (2.06 Å) is similarly shorter than that of NiSe (2.11 Å), which is consistent with the Fourier transform curves of Ni K-edge EXAFS in R space, suggesting a strong electronic interaction between NiSe and CNTs [9].

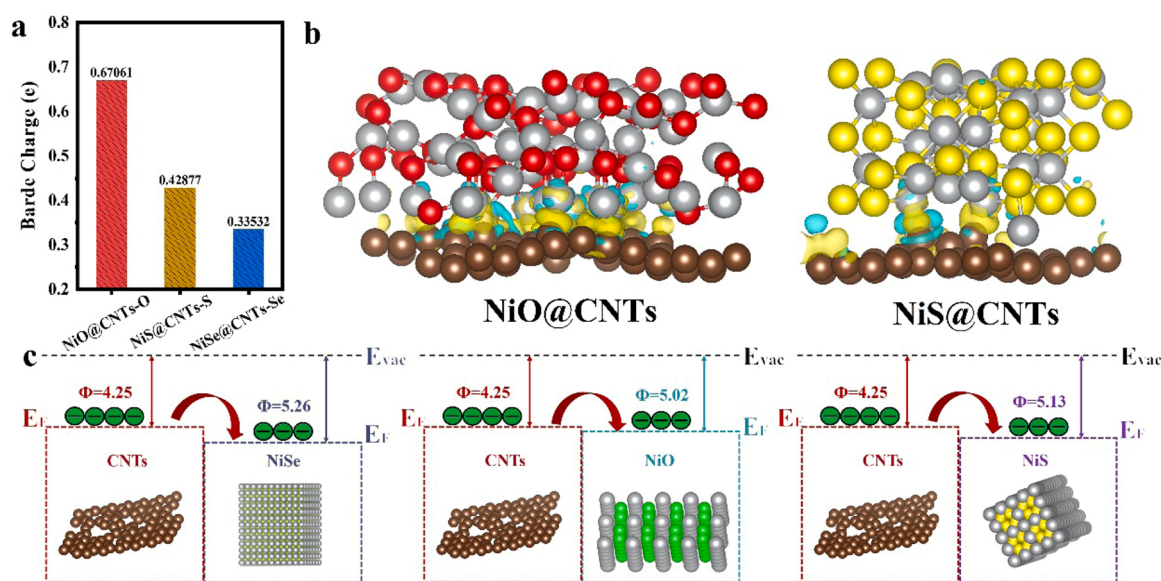


Fig. 2. (a) Bader charge of Se sites in NiSe@CNTs, O sites in NiO@CNTs and S sites in NiS@CNTs. (b) Charge density difference (CDD) of NiO@CNTs and NiS@CNTs. The yellow and blue regions represent electronic accumulation and depletion, respectively. (c) Schematic energy band diagrams of the NiSe@CNTs, NiO@CNTs and NiS@CNTs heterostructure and the Fermi level (E_F), work function (Φ) and vacuum level (E_{vac}) are also shown.

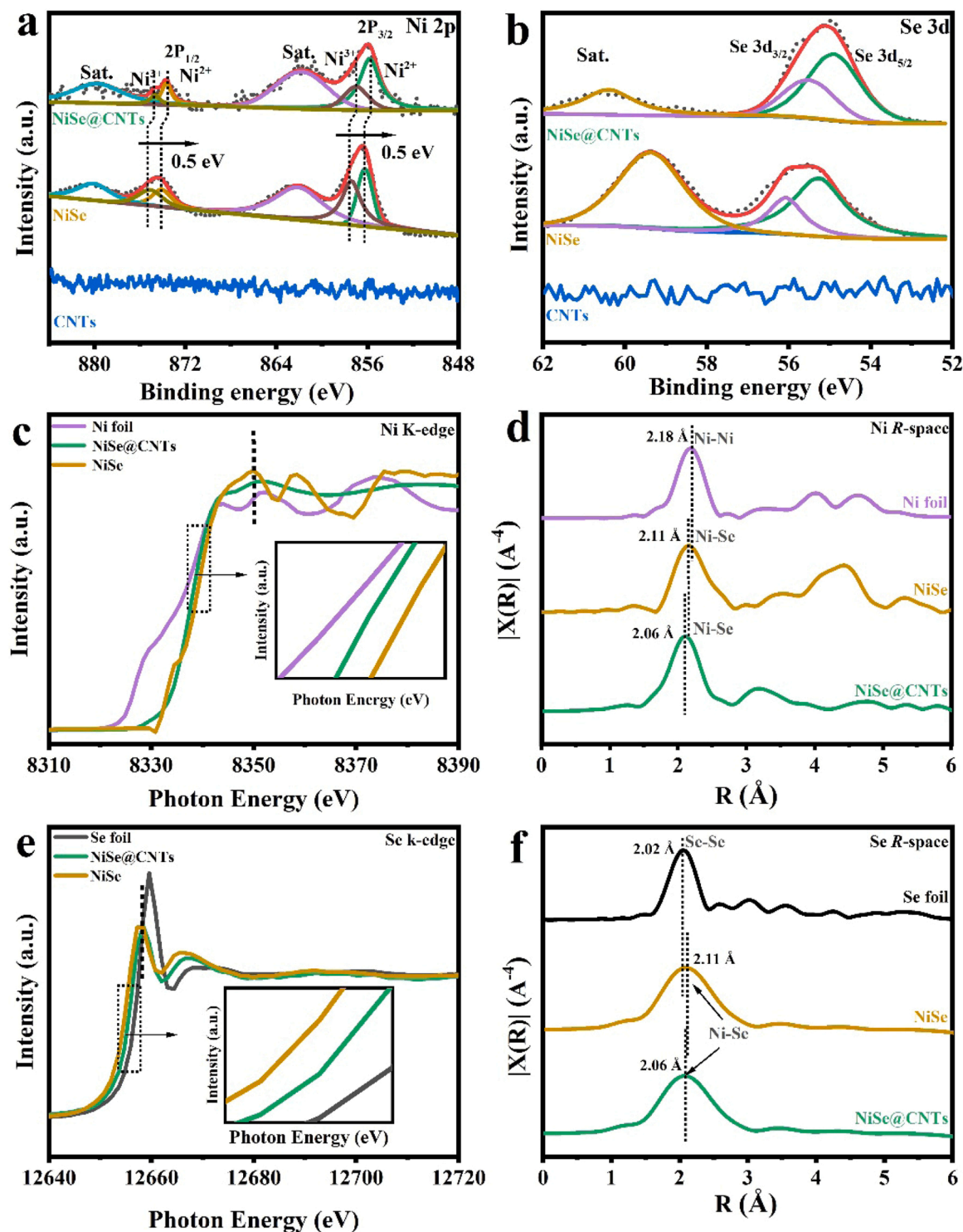


Fig. 3. XPS survey spectra of (a) Ni 2p and (b) Se 3d of NiSe, CNTs and NiSe@CNTs. (c) XANES Ni K-edge spectra and (d) Fourier transform curves of Ni K-edge EXAFS in R space of NiSe, NiSe@CNTs and Ni foil. (e) XANES Se K-edge spectra and (f) Fourier transform curves of Se K-edge EXAFS in R space of NiSe, NiSe@CNTs and Se foil.

The electrocatalytic performance of NiSe@CNTs was investigated in an N₂-saturated 1.0 M KOH solution with the aid of a typical three-electrode system [42]. The effect of the electrodeposition treatment time on their HER and OER electrocatalytic activity was firstly explored. It can be seen from Fig. S6-S7 that both HER and OER performance of NiSe@CNTs treated by electrodeposition for 800 s are the best. Fig. 4a displays iR-corrected HER LSV polarization curves of the optimal NiSe@CNTs, NiSe, Ni Foam and Pt/C counterparts [43]. To achieve the

current density of 10 mA cm⁻², the overpotential of NiSe@CNTs is only 27 mV, which is noteworthy smaller than those of NiSe (136 mV) and CNTs (199 mV), but more importantly also better than that of Pt/C (53 mV), indicating the HER activity enhancement through localization of d-electrons at the Ni sites after the construction of heterostructure (Table S2). The calculated Tafel slope can be used as an important reference to evaluate the HER kinetics and reaction mechanism of the above catalysts [44]. As illustrated in Fig. 4b, the Tafel slope of

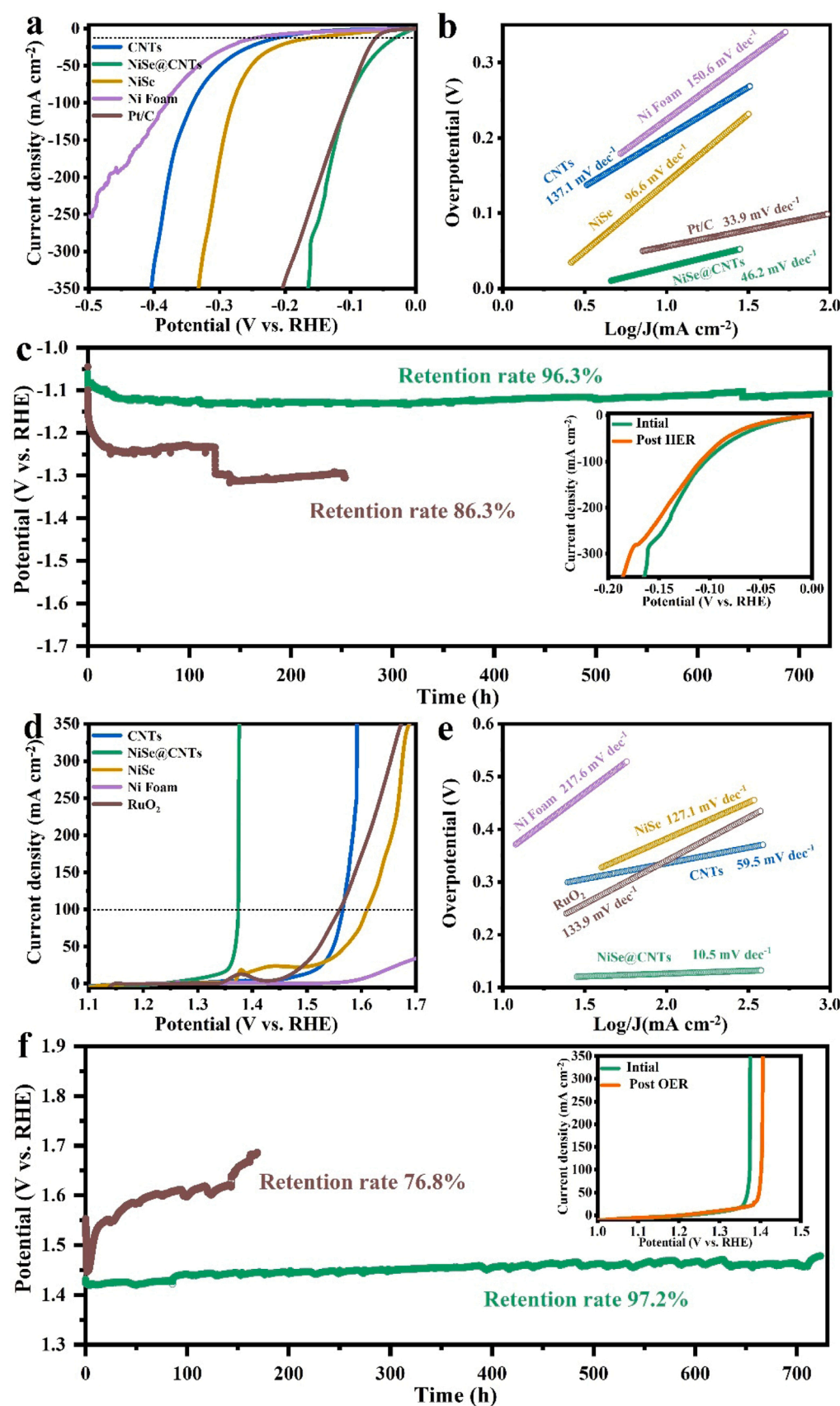


Fig. 4. (a) HER linear sweep voltammetry curves (LSVs) and (b) corresponding Tafel plots of Ni Foam, NiSe, CNTs, NiSe@CNTs and Pt/C in 1.0 M KOH solution. (c) HER stability measurement of NiSe@CNTs before and after stability testing. (d) OER LSVs and (e) corresponding Tafel plots of Ni Foam, NiSe, CNTs, NiSe@CNTs and RuO₂ in 1.0 M KOH solution. (f) OER stability test of NiSe@CNTs and RuO₂ as well as LSVs of NiSe@CNTs before and after stability testing.

NiSe@CNTs is only 46.2 mV dec^{-1} , which is significantly smaller than those of the NiSe ($137.1 \text{ mV dec}^{-1}$) and CNTs (96.6 mV dec^{-1}). The above results show that compared with these single-component catalysts, the optimal NiSe@CNTs catalyst possesses faster HER kinetics and higher catalytic activity. Furthermore, Therefore, it is also important to explore the stability of samples in addition to the activity. As shown in Fig. S8, the voltage retention of the NiSe catalyst is only 66.3% after 70 h operation, indicating poor catalytic stability due to nanoparticle agglomeration during the electrocatalytic reaction. Compared to the NiSe nanoparticle, the optimal NiSe@CNTs catalyst can achieve an impressive 96.3% voltage retention after more than a month-long

(upward of 730 h) stable operation under alkaline conditions which far exceeds that of commercial Pt/C (86.3% retention rate after 260 h). The inserted graph in Fig. 4c also shows that the polarization curve after HER largely overlaps with the initial one, indicating excellent stability. The XAENS and EXAFS curves of NiSe@CNTs after HER also confirm that there is no change in the electronic and local structures of the NiSe@CNTs after HER from the initial one, which further demonstrates excellent long-term stability (Fig. S9). As shown in the TEM images of the NiSe@CNTs catalyst after HER (Fig. S10a,b), the nanoparticles were confined to multiple intertwined carbon tubes and their heterogeneous structure was not disrupted.

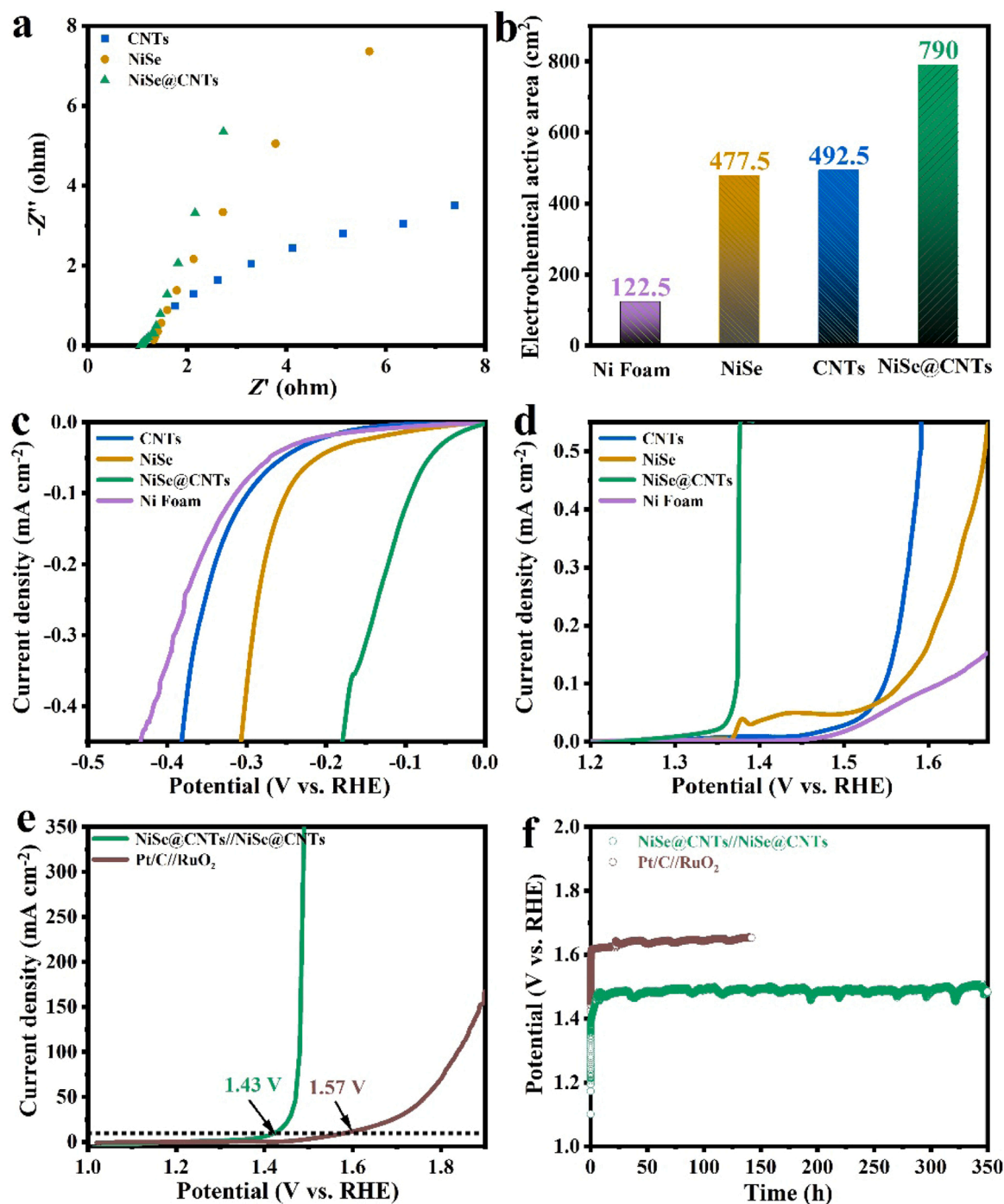


Fig. 5. (a) Nyquist plots of NiSe, CNTs and NiSe@CNTs. (b) ECSA values of Ni Foam, NiSe, CNTs and NiSe@CNTs. (c) HER polarization curves (d) OER polarization curves of Ni Foam, NiSe, CNTs and NiSe@CNTs after normalized by ECSA. (e) Overall water splitting polarization curves and (f) Corresponding chronoamperometry curve of NiSe@CNTs//NiSe@CNTs and Pt/C//RuO₂ in 1.0 M KOH electrolyte.

Even more appealingly, it is clear from Fig. 4d that the optimal NiSe@CNTs catalyst exhibits incredibly high electrocatalytic activity toward OER, with overpotential as low as 145 mV to achieve a large current density of 100 mA cm^{-2} , which is far superior to commercial RuO_2 (330 mV), NiSe (381 mV), CNTs (338 mV) and all currently reported state-of-the-art catalysts (Table S3). Meanwhile, its corresponding Tafel slope is the smallest value of 10.5 mV dec^{-1} among all as-prepared samples, revealing constructed heterostructure to enhance the OER kinetics of NiSe (Fig. 4e). Apart from its ultra-high OER activity, the NiSe@CNTs also exhibits amazing long-term stability in the oxygen evolution reaction. As shown in Fig. 4f, it exhibits negligible degradation after more than one month of stable OER operation under alkaline condition (97.2% retention rate over 730 h), which is significantly better than the RuO_2 (only 76.8% retention rate after 186 h). Additionally, the XAENS and EXAFS curves of NiSe@CNTs after OER also show that there is no change in the electronic and local structures of the NiSe@CNTs after OER from the initial one, which further demonstrates excellent long-term stability (Fig. S12). It can be seen from the TEM images (Fig. S13a,b) of the NiSe@CNTs catalyst after the OER that the NiSe nanoparticles are firmly anchored to the carbon tubes and their heterogeneous structure is not damaged. Moreover, the HAADF-EDX element mapping images (Fig. S13c) further demonstrate that its morphology and elemental composition do not change substantially before and after the OER test for 1000 cycles. This indicates that the NiSe@CNTs catalyst exhibits excellent stability by benefiting from the strong interaction between the NiSe and CNTs. The unparalleled ultra-high stability can be attributed to: (1) The introduced CNTs firmly grip the NiSe nanoparticles to avoid agglomeration between them, which effectively prevents the number of Ni active sites from being masked, thus greatly ensuring its high electrocatalytic activity. (2) The CNTs encapsulated on the outside of the NiSe nanoparticles effectively reduce the damage caused by the alkaline solution and the external environment.

Next, the improvement mechanism of catalytic performance was further investigated by electrochemical tests. Electrical impedance spectroscopy (EIS) was used to evaluate the charge transfer kinetics of the as-prepared samples [45]. As shown in Fig. 5a, NiSe@CNTs catalyst exhibits lower internal resistance and faster fast charge transfer than single species (NiSe and CNTs) due to the localized electronic states, suggesting that the heterogeneous structure constructed by NiSe and CNTs possesses relatively high carrier mobility across the Helmholtz layer (the electrode/electrolyte interface). To further analyze the enhanced electrocatalytic activity of NiSe@CNTs, we calculated the electrochemical active surface area (ECSA) with the help of the measured electrochemical double-layer capacitance (C_{dl}) [46]. In theory, the ECSA value refers to the part that plays a catalytic role, then a larger ECSA means that more active sites are available for HER and OER reactions, thus favoring the adsorption of water molecules and close contact with the electrolyte [47]. Fig. S14-S16 shows the CV curves of all as-prepared samples recorded at the same potential region at scan rates from 20 to 100 mV s^{-1} . As displayed in Fig. 5b, the NiSe@CNTs catalyst possesses the largest ECSA value of 790 cm^2 , which is higher than that of NiSe (477.5 cm^2) and CNTs (492.5 cm^2). Fig. 5c-d present that the specific activities for HER and OER of the NiSe@CNTs are significantly higher than that of the single species (NiSe and CNTs), which is in agreement with the results of morphological characterization. In order to identify the real active sites on the NiSe@CNTs, thiocyanate ions (SCN^-), an active site toxin of metal samples, were added to the 1.0 M KOH electrolyte [43]. As shown in Fig. S 18, the SCN^- addition dramatically reduces the activity of the NiSe@CNTs catalyst, indicating that the Ni sites on the NiSe@CNTs are the real active sites for HER and OER catalysis. It is well known that mass activity is closely related to the cost of practical applications [48]. In order to evaluate the mass activity of samples, their mass activities are evaluated by normalizing the polarization curve to the mass of the catalyst. As shown in Fig. S17a, the optimal NiSe@CNTs catalyst exhibits higher mass activity than NiSe and

CNTs under alkaline electrolyte. Furthermore, Fig. S17b displays that its mass activity for OER is significantly higher than that of the single species NiSe and CNTs under alkaline electrolyte.

The above-mentioned analysis further confirms that the constructed heterogeneous structure modulates the electron density of the real Ni active sites to promote intrinsic activity.

Benefiting from the unparalleled bifunctional electrocatalytic performance of NiSe@CNTs, the overall water-splitting performance was investigated by a two-electrode system [49]. As expected, the two-electrode system of NiSe@CNTs requires an ultra-low potential of 1.43 V to achieve a current density of 10 mA cm^{-2} (Fig. 5e). Its overall water splitting performance is dramatically better than that of commercial Pt/C// RuO_2 and even surpasses those of almost all recently reported catalysts (Table S4). In addition, the stability test results show that the NiSe@CNTs did not exhibit a significant voltage drop after 350 h of stable operation (Fig. 5f). In summary, the above series of electrochemical analysis results reflect that the optimal NiSe@CNTs catalyst possesses great application in the field of electrochemical water splitting.

To exploit the augment mechanism of OER and HER on NiSe by introducing CNTs, density functional theory (DFT) calculations were performed [50]. Considering the strong electron interaction between NiSe and CNTs, which can regulate the electronic distribution of NiSe, we modeled NiSe-Ni, NiSe-Se, NiSe@CNTs-Ni and NiSe@CNTs-Se (Fig. S19 and Fig. 6a-b) to further investigate the OER and HER process. As shown in Fig. 6c-d, the free energy change of OER and HER was calculated on Ni and Se sites. Fig. 6c displays an endothermic process of OER, where the proton/electron-transferring step with the most positive free energy change is the rate-determining step (RDS), limiting the proceed of OER [51]. We found that it has a common RDS in the $^*\text{OOH}$ formation step with an overpotential of 0.42 and 1.29 V, respectively, indicative of better OER behavior of Ni compared with Se sites. With the recombination of CNTs, the Ni and Se sites in NiSe@CNTs deliver OER improvement with an overpotential of 0.34 and 0.93 V, respectively, together with RDS change from $^*\text{OOH}$ formation to $^*\text{OH}$ - $^*\text{O}$ conversion. Besides, in the HER process, the Ni sites in NiSe@CNTs display optimal HER activity with $^*\text{H}$ adsorption of -0.17 eV , closest to 0 eV of ideal HER catalysts (Fig. 6d). The following order in $^*\text{H}$ adsorption is NiSe-Ni (0.36 eV), NiSe-Se (0.53 eV), and NiSe@CNTs-Se (-0.99 eV), respectively. This certifies the effect of CNTs interfaced with NiSe in improving OER and HER on Ni sites. In addition, we calculated the free energy for the OER reaction of Ni-based oxide or hydroxide (NiOOH@CNTs and NiO@CNTs) to further clarify the real active species. The optimized adsorption structures of the reaction intermediates ($^*\text{OH}$, $^*\text{O}$, $^*\text{OOH}$) on the catalyst surface were provided in Fig. S22a-b. As shown in Fig. S22c, with the recombination of CNTs, the Ni sites in NiSe@CNTs, NiOOH@CNTs and NiO@CNTs deliver OER improvement with an overpotential of 0.34, 0.68 and 1.48 V, respectively. The above calculations show that the activity of NiOOH and NiO is much lower than that of NiSe, which further proves that NiSe is the main active substance.

The catalytic activity is highly dependent on the regulation of electronic structure [52]. we calculated the Bader charge of Ni sites in the NiSe@CNTs-Ni (Fig. 6e). In comparison with NiSe (NiSe-B, NiSe-A), The positive charges states of Ni atoms in bulk layer L_2 and active sites increase while that of Ni atoms in interface layers L_1 decrease, certifying the electronic assemble in the interface between carbon and Ni layers, agreeing with charge density difference. Furthermore, the work function of Ni atoms in L_1 is higher than in L_2 and A_3 , showing an electronic transfer from L_2 and A_3 to L_1 , which can tailor the electronic density of surface Ni sites (Fig. 6f). As shown in Fig. 6g, by this electronic gathering in the interface, it leads to the shift of DOS towards a higher energy level, exhibiting more states in the Fermi states and electronic conductivity. As expected, the Ni sites of the NiSe@CNTs are closer to the Fermi energy level compared to those with NiSe, which directly confirms that the heterostructure can activate the activity of the Ni sites, in agreement with the systematic characterization and calculations results. In sum, the

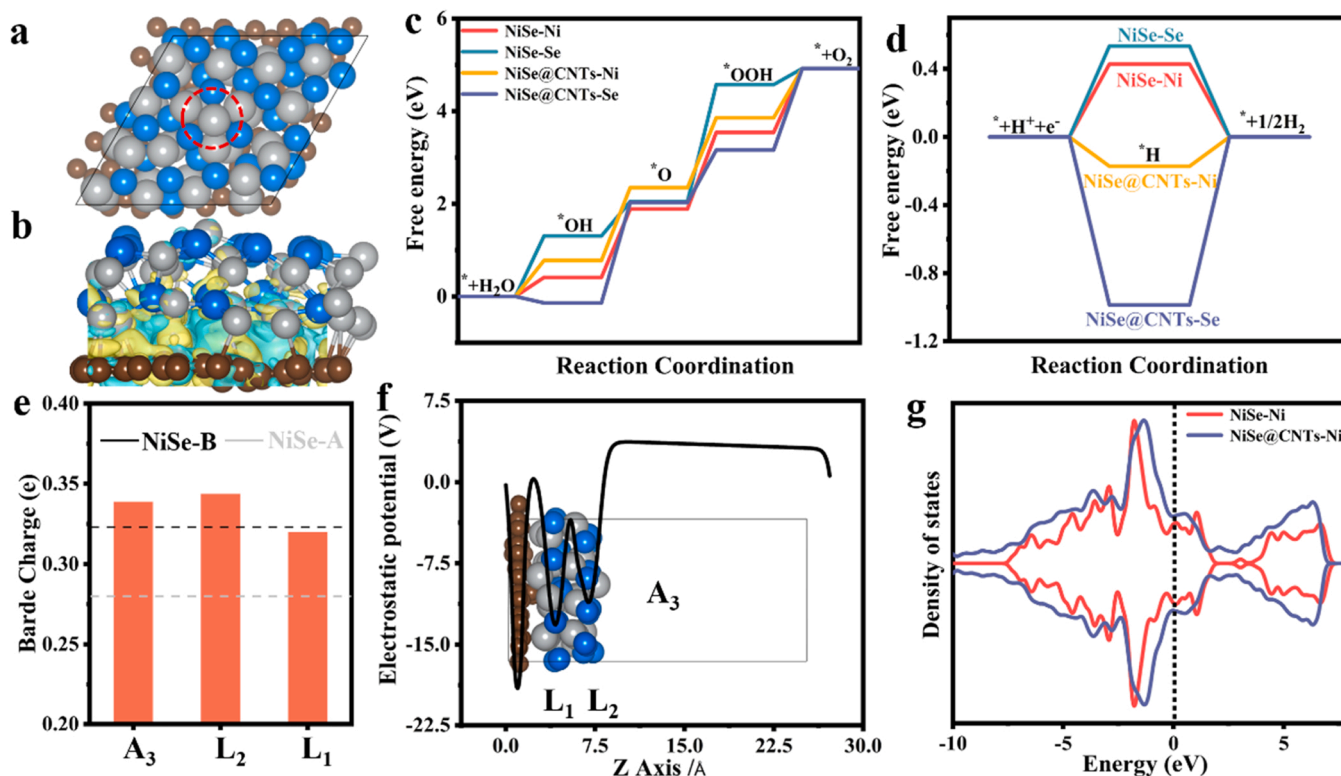


Fig. 6. (a) Optimized models of NiSe@CNTs. The brown, grey and blue balls represent the C, Ni, and Se atoms, respectively. (b) CDD of NiSe@CNTs-Ni. The yellow and blue regions represent electronic accumulation and depletion, respectively. The free energy profile along OER (c) and HER (d) on Ni or Se sites. (e) Bader charge of Ni atom in NiSe@CNTs-Ni relative to NiSe. The A and B denote the active sites and bulk atoms, respectively. (f) the work function distribution of NiSe@CNTs-Ni. The L₁, L₂ and A₃ denote the interfacial Ni layer, bulk Ni layers and Active sites, respectively. (g) The density of states of NiSe@CNTs-Ni and NiSe-Ni.

electronic gathering effect activates the surface Ni activity, which promotes the HER and OER activity.

4. Conclusion

In summary, we selected CNTs with a large number of π -electrons delocalization to construct heterostructures with NiSe to tune the electronic structure of the Ni sites, thus stimulating the hidden catalytic potential of the Ni sites. XPS, XAS and Bader charge results show that the electron density of the Ni site is significantly increased with the help of π -electron delocalization of the CNTs. DFT calculations further confirmed that the excited Ni not only greatly optimizes the H^* adsorption kinetics, but also lowers the energy barrier for the rate-determining step ($*O \rightarrow *OOH$), demonstrating the intrinsic catalytic activity enhancement of the NiSe@CNTs. In addition, the introduced CNTs not only avoid aggregation of nanoparticles but also reduce their particle size, which increases the number of exposed Ni active sites. As expected, the constructed NiSe@CNTs is considered to be an unprecedentedly high activity and robust HER/OER electrocatalyst in alkaline media, outperforming commercial Pt/C, RuO₂ and almost all of the recently reported advanced catalysts. NiSe@CNTs as bifunctional catalysts exhibit efficient water splitting in a two-electrode system, with a cell voltage of only 1.43 V at 10 mA cm⁻² and outstanding long-term stability of 350 h.

CRedit authorship contribution statement

Hongyao Xue: Conceptualization, Investigation, Writing – original draft, Funding acquisition. **Tongqing Yang:** Methodology, Investigation. **Ziming Zhang:** Methodology, Software. **Yixue Zhang:** Writing – review & editing, Funding acquisition. **Zhihong Geng:** Investigation. **Yan He:** Writing – review, Supervision, Funding acquisition.

Declaration of Competing Interest

The authors declare that they have no known competing financial interests or personal relationships that could have appeared to influence the work reported in this paper.

Data availability

No data was used for the research described in the article.

Acknowledgment

The authors gratefully acknowledge financial support from the National Natural Science Foundation of China (No. 52176076, 51676103), Taishan Scholar Project of Shandong Province (China) (No. ts20190937), Natural Science Foundation of Shandong Province (China) (No. ZR2021QE007, ZR2021LFG003) and Qingdao Postdoctoral Science Foundation (No. QDBSH20220201021, QDBSH20220202084). We would like to thank Zhang Jing from Shiyanjia Lab (www.shiyanjia.com) for the XPS analysis, Shenzhen HUASUAN Technology Co., Ltd. and beamline BL14W1 (Shanghai Synchrotron Radiation Facility) for providing the beam time.

Appendix A. Supporting information

Supplementary data associated with this article can be found in the online version at [doi:10.1016/j.apcatb.2023.122641](https://doi.org/10.1016/j.apcatb.2023.122641).

References

- [1] A.L. Li, S. Kong, C.X. Guo, H. Ooka, K. Adachi, D. Hashizume, Q.K. Jiang, H.X. Han, J.P. Xiao, R. Nakamura, Enhancing the stability of cobalt spinel oxide towards sustainable oxygen evolution in acid, *Nat. Catal.* 5 (2022) 109–118.

- [2] N.Y. Du, C. Roy, R. Peach, M. Turnbull, S. Thiele, C. Bock, Anion-exchange membrane water electrolyzers, *Chem. Rev.* 122 (2022) 11830–11895.
- [3] B.K. Kim, M.J. Kim, J.J. Kim, Modulating the active sites of nickel phosphorous by pulse-reverse electrodeposition for improving electrochemical water splitting, *Appl. Catal. B: Environ.* 308 (2022), 121226.
- [4] S.T. Wen, J. Huang, T.T. Li, W. Chen, G.L. Chen, Q. Zhang, X.H. Zhang, Q.Y. Qian, K. Ostrikov, Multiphase nanosheet-nanowire cerium oxide and nickel-cobalt phosphide for highly-efficient electrocatalytic overall water splitting, *Appl. Catal. B: Environ.* 316 (2022), 121678.
- [5] F.T. Haase, A. Bergmann, T.E. Jones, J. Timoshenko, A. Herzog, H.S. Jeon, C. Rettenmaier, B.R. Cuenya, Size effects and active state formation of cobalt oxide nanoparticles during the oxygen evolution reaction, *Nat. Energy* 7 (2022) 765–773.
- [6] Y.S. Chen, J.K. Wang, Z.B. Yu, Y.P. Hou, R.H. Jiang, M. Wang, J. Huang, J.H. Chen, Y.Q. Zhang, H.X. Zhu, Functional group scission-induced lattice strain in chiral macromolecular metal-organic framework arrays for electrocatalytic overall water splitting, *Appl. Catal. B: Environ.* 307 (2022), 121151.
- [7] Q. Wang, H. Xu, X.Y. Qian, G.Y. He, H.Q. Chen, Sulfur vacancies engineered self-supported Co_3S_4 nanoflowers as an efficient bifunctional catalyst for electrochemical water splitting, *Appl. Catal. B: Environ.* 322 (2023), 122104.
- [8] Y. Wang, X.P. Li, M.M. Zhang, J.F. Zhang, Z.L. Chen, X.R. Zheng, Z.L. Tian, N. Q. Zhao, X.P. Han, K.R. Zaghbi, Y.S. Wang, Y.D. Deng, W.B. Hu, Highly Active and Durable Single-Atom Tungsten-Doped $\text{Ni}_{0.5}\text{Se}_{0.5}$ Nanosheet@ $\text{Ni}_{0.5}\text{Se}_{0.5}$ Nanorod Heterostructures for Water Splitting, *Adv. Mater.* 34 (2022) 2107053.
- [9] K. Srinivas, F. Ma, Y.F. Liu, Z.H. Zhang, Y. Wu, Y.F. Chen, Metal-organic framework-derived Fe-doped $\text{Ni}_3\text{Se}_4/\text{NiSe}_2$ heterostructure-embedded mesoporous tubes for boosting oxygen evolution reaction, *ACS Appl. Mater. Interfaces* 14 (2022) 52927–52939.
- [10] X.Q. Wang, J.R. He, B. Yu, B.C. Sun, D.X. Yang, X.J. Zhang, Q.H. Zhang, W. L. Zhang, L. Gu, Y.F. Chen, CoSe_2 nanoparticles embedded MOF-derived Co-N-C nanoflake arrays as efficient and stable electrocatalyst for hydrogen evolution reaction, *Appl. Catal. B: Environ.* 258 (2019), 117996.
- [11] X. Chen, X.Q. Wang, X.J. Zhang, D.W. Liu, K. Srinivas, F. Ma, B. Wang, B. Yu, Q. Wu, Y.F. Chen, Facile and scalable synthesis of heterostructural $\text{NiSe}_2/\text{FeSe}_2$ nanoparticles as efficient and stable binder-free electrocatalyst for oxygen evolution reaction, *Int. J. Hydrog. Energy* 46 (2021) 35198–35208.
- [12] S.M.N. Jeghan, D. Kim, Y. Lee, M. Kim, G. Lee, Designing a smart heterojunction coupling of cobalt-iron layered double hydroxide on nickel selenide nanosheets for highly efficient overall water splitting kinetics, *Appl. Catal. B: Environ.* 308 (2022), 122121.
- [13] L.L. Zhai, T.W.B. Lo, Z.L. Xu, J. Potter, J.Y. Mo, X.Y. Guo, C.C. Tang, S.C.E. Tsang, S.P. Lau, In situ phase transformation on nickel-based selenides for enhanced hydrogen evolution reaction in alkaline medium, *ACS Energy Lett.* 5 (2020) 2483–2491.
- [14] Y.J. Chen, Z.Y. Ren, H.Y. Fu, X. Zhang, G.H. Tian, H.G. Fu, $\text{NiSe-Ni}_{0.85}\text{Se}$ Heterostructure Nanoflake Arrays on Carbon Paper as Efficient Electrocatalysts for Overall Water Splitting, *Small* 14 (2018) 1800763.
- [15] K.L. Guo, Y.T. Wang, S.Z. Yang, J.F. Huang, Z.H. Zou, H.R. Pan, P.S. Shinde, S. L. Pan, J.E. Huang, C.L. Xu, Bonding interface boosts the intrinsic activity and durability of $\text{NiSe}/\text{Fe}_2\text{O}_3$ heterogeneous electrocatalyst for water oxidation, *Sci. Bull.* 66 (2022) 52–61.
- [16] J.Y. Xue, F.L. Li, B.B. Chen, H.B. Geng, W. Zhang, W.Y. Xu, H.W. Gu, P. Braunstein, J.P. Lang, Engineering multiphase $\text{MoSe}_2/\text{NiSe}$ heterostructure interfaces for superior hydrogen production electrocatalysis, *Appl. Catal. B: Environ.* 312 (2022), 121434.
- [17] N. Shaikh, I. Mukhopadhyay, A. Ray, Heterointerfaces of nickel sulphides and selenides on Ni-foam as efficient bifunctional electrocatalysts in acidic environments, *J. Mater. Chem. A* 10 (2022) 12733.
- [18] D.Y. He, L.Y. Cao, J.F. Huang, Y.Q. Feng, G.D. Li, D. Yang, Q.Q. Huang, L.L. Feng, Rational Design of Vanadium-Modulated Ni_3Se_2 Nanorod@Nanosheet Arrays as a Bifunctional Electrocatalyst for Overall Water Splitting, *ACS Sustain. Chem. Eng.* 35 (2021) 12005–12016.
- [19] Y. Li, Y. Zhao, F.M. Li, Z.Y. Dang, P.Q. Gao, Ultrathin NiSe Nanosheets on Ni Foam for Efficient and Durable Hydrazine-Assisted Electrolytic Hydrogen Production, *ACS Appl. Mater. Interfaces* 13 (2021) 34457–34467.
- [20] K. Chang, D.T. Tran, J.Q. Wang, N.H. Kim, J.H. Lee, A 3D hierarchical network derived from 2D Fe-doped NiSe nanosheets/carbon nanotubes with enhanced OER performance for overall water splitting, *J. Mater. Chem. A* 10 (2022) 3102.
- [21] Y.J. Son, S. Kim, V. Leung, K. Kawashima, J. Noh, K. Kim, R.A. Marquez, O.A. C. Jaim, L.A. Smith, H. Celio, D.J. Milliron, B.A. Korgel, C.B. Mullins, Effects of Electrochemical Conditioning on Nickel-Based Oxygen Evolution Electrocatalysts, *ACS Catal.* 12 (2022) 10384–10399.
- [22] B. Zhao, J.W. Liu, C.Y. Xu, R.F. Feng, P.F. Sui, L. Wang, J.J. Zhang, J.L. Luo, X. Z. Fu, Hollow NiSe nanocrystals heterogenized with carbon nanotubes for efficient electrocatalytic methanol upgrading to boost hydrogen co-production, *Adv. Funct. Mater.* 31 (2020), 208812.
- [23] R. Ihly, K.S. Mistry, A.J. Ferguson, T.T. Clikeman, B.W. Larson, O. Reid, O. V. Boltalina, S.H. Strauss, G. Rumbles, J.L. Blackburn, Tuning the driving force for exciton dissociation in single-walled carbon nanotube heterojunctions, *Nat. Chem.* 8 (2016) 603–609.
- [24] K.J. Chen, M.Q. Cao, G.H. Ni, S.Y. Cheng, H.X. Liao, L. Zhu, H.M. Li, J.W. Fu, J. H. Hu, E. Cortes, M. Liu, Nickel polyphthalocyanine with electronic localization at the nickel site for enhanced CO_2 reduction reaction, *Appl. Catal. B: Environ.* 306 (2022), 121093.
- [25] T. Ouyang, Y.Q. Liu, C.Y. Wu, K. Xiao, Z.Q. Liu, Heterostructures Composed of N-Doped Carbon Nanotubes Encapsulating Cobalt and $\beta\text{-Mo}_2\text{C}$ Nanoparticles as Bifunctional Electrodes for, in: *Angew Water Splitting* (Ed.), Chem. Int., 58, 2019, pp. 4923–4928.
- [26] W.L. Lu, J.B. Cui, R. Jiang, Y.G. Chen, L.Y. Wang, In-situ wet tearing based subnanometer MoSeS for efficient hydrogen evolution, *Sci. China Mater.* 60 (2017) 929–936.
- [27] C.Y. Cai, Y. Ma, J. Jeon, F. Huang, F.X. Jia, S. Lai, Z.H. Xu, C.J. Wu, R.Q. Zhao, Y. F. Hao, Y.Q. Chen, S.J. Lee, M. Wang, Epitaxial growth of large-grain NiSe films by solid-state reaction for high-responsivity photodetector arrays, *Adv. Mater.* 29 (2017) 1606180.
- [28] J. Duan, A.B. Chen, S.L. Hou, J. Guan, CNT modified by mesoporous carbon anchored by Ni nanoparticles for CO_2 electrochemical reduction, *Carbon Energy* 4 (2022) 1274–1284.
- [29] W.Z. Huang, J.T. Li, X.B. Liao, R.H. Lu, C.H. Ling, X. Liu, J.S. Meng, L.B. Qu, M. T. Lin, X.F. Hong, X.B. Zhou, S.L. Liu, Y. Zhao, L. Zhou, L.Q. Mai, Ligand modulation of active sites to promote electrocatalytic oxygen evolution, *Adv. Mater.* 34 (2022) 2200270.
- [30] L. Chen, Y. Ha, R.R. Wang, Y.X. Liu, H.B. Xu, B. Shang, R.B. Wu, H.G. Pan, Inner Co Synergizing Outer Ru Supported on Carbon Nanotubes for Efficient pH-Universal Hydrogen Evolution Catalysis, *Nano-Micro Lett.* 14 (2022) 186.
- [31] Z.Y. Cai, P. Wang, J.J. Zhang, A.Y. Chen, J.W. Zhang, Y. Yan, X.Y. Wang, Reinforced layered double hydroxide oxygen-evolution electrocatalysts: a polyoxometallic acid wet-etching approach and synergistic mechanism, *Adv. Mater.* 34 (2022) 2110696.
- [32] L.J. Zhang, W.W. Cai, N.Z. Bao, H. Yang, Implanting an electron donor to enlarge the D-P hybridization of high-entropy (Oxy)hydroxide: a novel design to boost oxygen evolution, *Adv. Mater.* 34 (2022) 2110511.
- [33] C.J. Lyu, J.R. Chen, K.L. Wu, J.W. Wu, N. Wang, Z.L. Guo, P.F. Hu, W.M. Lau, J. L. Zheng, Interfacial electronic structure modulation of CoP nanowires with FeP nanosheets for enhanced hydrogen evolution under alkaline water/ seawater electrolytes, *Appl. Catal. B: Environ.* 317 (2022), 121799.
- [34] H.Y. Xue, A.L. Meng, H.Q. Zhang, Y.S. Lin, Z.J. Li, C.S. Wang, 3D urchin like V-doped CoP in situ grown on nickel foam as bifunctional electrocatalyst for efficient overall water-splitting, *Nano Res* 14 (2021) 4173–4181.
- [35] H.Y. Xue, A.L. Meng, T.Q. Yang, Z.J. Li, C.J. Chen, Controllable oxygen vacancies and morphology engineering: ultra-high HER/OER activity under base-acid conditions and outstanding antibacterial properties, *J. Energy Chem.* 71 (2022) 639–651.
- [36] Y. Wang, Y.Z. Zhao, L. Liu, W.J. Qin, S.J. Liu, J.P. Tu, Y.P. Qin, J.F. Liu, H.Y. Wu, D. Y. Zhang, A.M. Chu, B.R. Jia, X.H. Qu, M.L. Qin, Mesoporous Single Crystals with Fe-Rich Skin for Ultralow Overpotential in Oxygen Evolution Catalysis, *Adv. Mater.* 34 (2022), 220008.
- [37] D. Shao, Q. Wang, X.Z. Yao, Y.T. Zhou, X.Y. Yu, Phase-engineering of nickel hydroxide in the $\text{Ni}/\text{Ni}(\text{OH})_2$ interface for efficient hydrogen evolution and hydrazine-assisted water splitting in seawater, *J. Mater. Chem. A* 10 (2022) 21848–21855.
- [38] H.C. Sun, L.F. Li, H.C. Chen, D.L. Duan, M. Humayun, Y. Qiu, X. Zhang, X. Ao, Y. Wu, Y.J. Pang, K.F. Huo, C.D. Wang, Y.J. Xiong, Highly efficient overall urea electrolysis via single-atomically active centers on layered double hydroxide, *Sci. Bull.* 67 (2022) 1763–1775.
- [39] R.Y. Zeng, C.C. Cheng, F.S. Xing, Y. Zou, K.N. Ding, C.J. Huang, Dual vacancies induced local polarization electric field for high-performance photocatalytic H_2 production, *Appl. Catal. B: Environ.* 316 (2022), 121680.
- [40] Z.Y. Shao, Q. Zhu, Y. Sun, Y. Zhang, Y.L. Jiang, S.Q. Deng, W. Zhang, K.K. Huang, S.H. Feng, Phase-Reconfiguration-Induced $\text{NiS}/\text{NiFe}_2\text{O}_4$ Composite for Performance-Enhanced Zinc–Air Batteries, *Adv. Mater.* 34 (2022) 2110172.
- [41] K. Jiang, B.Y. Liu, M. Luo, S.C. Ning, M. Peng, Y. Zhao, Y.R. Lu, T.S. Chan, F.M. de Groot, Y.W. Tan, Single platinum atoms embedded in nanoporous cobalt selenide as electrocatalyst for accelerating hydrogen evolution reaction, *Nat. Commun.* 10 (2019) 1743.
- [42] Y.J. Huang, M.L. F. Pan, Z.Y. Zhu, H.M. Sun, Y.W. Tang, G.T. Fu, Plasma-induced Mo-doped Co_3O_4 with enriched oxygen vacancies for electrocatalytic oxygen evolution in water splitting, *Carbon Energy* (2022), <https://doi.org/10.1002/cey2.2>.
- [43] D.H. Kweon, M.S. Okyay, S.J. Kim, J.P. Jeon, H.J. Noh, N. Park, J. Mahmood, J. B. Baek, Ruthenium anchored on carbon nanotube electrocatalyst for hydrogen production with enhanced Faradaic efficiency, *Nat. Commun.* 11 (2020) 1278.
- [44] H.Y. Xue, A.L. Meng, C.C. Chen, H.Y. Xue, Z.J. Li, C.S. Wang, Phosphorus-doped MoS_2 with sulfur vacancy defects for enhanced electrochemical water splitting, *Sci. China Mater.* 65 (2022) 712–720.
- [45] T.Y. Xu, D.X. Jiao, M.M. Liu, L. Zhang, X.F. Fan, L.R. Zheng, W.T. Zheng, X.Q. Cui, Ni Center Coordination Reconstructed Nanocorals for Efficient Water Splitting, *Adv. Sci.* 34 (2022) 2205605.
- [46] H.Q. Song, J.K. Yu, Z.Y. Tang, B. Yang, S.Y. Lu, Halogen-doped carbon dots on amorphous cobalt phosphide as robust electrocatalysts for overall water splitting, *Adv. Energy Mater.* 12 (2022) 2102573.
- [47] Y.D. Liu, Y. Chen, Y.H. Tian, T. Sakthivel, H. Liu, S.W. Guo, H.B. Zeng, Z.F. Dai, Synergizing hydrogen spillover and deprotonation by the internal polarization field in a $\text{MoS}_2/\text{NiPS}_3$ vertical heterostructure for boosted water electrolysis, *Adv. Mater.* 34 (2022) 2203615.
- [48] F. Li, M.H. Kweon, G.F. Han, H.J. Noh, W. Chen, I. Ahmad, J.P. Jeon, Z.P. Fu, Y. L. Lu, J.B. Baek, Merging platinum single atoms to achieve ultrahigh mass activity and low hydrogen production cost, *ACS Nano* 17 (2023) 2923–2931.
- [49] Q. Gao, W. Luo, X.Y. Ma, Z.M. Ma, S.J. Li, F.L. Guo, W. Shen, Y.M. Jiang, R.X. He, M. Li, Electronic modulation and vacancy engineering of Ni_9S_8 to synergistically boost efficient water splitting: Active vacancy-metal pairs, *Appl. Catal. B: Environ.* 310 (2022), 121356.

- [50] M. Ramadoss, Y.F. Chen, Y. Hu, B. Wang, R. Jeyagopal, K. Marimuthu, X.Q. Wang, D.X. Yang, Hierarchically porous nanoarchitecture constructed by ultrathin CoSe₂ embedded Fe-CoO nanosheets as robust electrocatalyst for water oxidation, *J. Mater. Sci. Technol.* 78 (2021) 229–237.
- [51] J.H. Zhou, Z.G. Wang, D.X. Yang, F. Qi, X. Hao, W.L. Zhang, Y.F. Chen, NiSe₂-anchored N, S-doped graphene/Ni foam as a free-standing bifunctional electrocatalyst for efficient water splitting, *Nanoscale* 12 (2020) 9866–9872.
- [52] M. Lu, Y. Zheng, Y. Hu, B.L. Huang, D.G. Ji, M.Z. Sun, J.Y. Li, Y. Peng, R. Si, P.X. Xi, C.H. Yan, Artificially steering electrocatalytic oxygen evolution reaction mechanism by regulating oxygen defect contents in perovskites, *Sci. Adv.* 8 (2022) eabq3563.